CrossMark

High-throughput optimization of near-infrared-transparent Mo-doped In$_2$O$_3$ thin films with high conductivity by combined use of atmospheric-pressure mist chemical-vapor deposition and sputtering

Naoomi Yamada *, Masayoshi Yamada, Haruna Toyama, Ryuichiro Ino, Xiang Cao, Yuuki Yamaguchi, Yoshihiko Ninomiya

Department of Applied Chemistry, Chubu University, 1200 Matsumoto, Kasugai, Aichi 487-8501, Japan

ARTICLE INFO

ABSTRACT

Thin films of near-infrared (NIR)-transparent and highly conductive Mo-doped In$_2$O$_3$ (IMO) were prepared as transparent electrodes in thin-film photovoltaic cells and energy-efficient windows. The fabrication process was rapidly optimized by the combined use of atmospheric-pressure mist chemical-vapor deposition (mist-CVD) and sputtering. Mist-CVD was used to rapidly deposit IMO thin films with various Mo-dopant concentrations. We obtained highly conductive IMO thin films with transmittance above 70% in a wide wavelength range of 0.3–2.5 μm when the Mo-dopant concentration was ~1 at% and the Mo dopants had an oxidation state of +4. The IMO films with the optimum Mo-dopant concentration of ~1 at% had low resistivities of $(3–4) \times 10^{-4}$ Ω cm resulting from high electron mobilities exceeding 80 cm^2 V^{-1} s^{-1} and suppressed electron densities of $(2–3) \times 10^{-4}$ cm^{-3}, which prevented the degradation of transparency in the NIR region. We applied these findings to the growth of IMO thin films by sputter deposition, which is readily extendable from laboratory scale to industrial scale. As a result, a high-performance IMO film was successfully obtained in only a few deposition runs. The optimized sputtered IMO film exhibited an extraordinarily high electron mobility of 93 cm^2 V^{-1} s^{-1} and relatively low electron density of 1.5×10^{20} cm^{-3}, leading to a plasma wavelength that was longer than 4 μm. This optimized IMO film allowed passage of the full solar spectrum and exclusively reflected far-infrared light corresponding to thermal radiation at room temperature, allowing it to be used as transparent electrodes in photovoltaic cells and heat-reflective electrodes in energy-efficient electrochromic windows. We believe the combination of mist-CVD and sputtering can be extended to rapid optimization of other functional oxide systems.

1. Introduction

Photovoltaic cells represent a key approach to realizing a sustainable source of energy. Thus, considerable efforts have been made to develop high-efficiency photovoltaic cells. One of the important components of thin-film photovoltaic cells is the transparent-conducting-oxide (TCO) electrode. The optoelectronic performance of TCO substantially affects the cells' photovoltaic conversion efficiency. Since the bandgap (E_g) of major photovoltaic absorber materials, including Si ($E_g = 1.1$ eV) and CuInSe$_2$ ($E_g = 1.0$ eV), corresponds to the wavelength of light in the near-infrared range (1.1–1.2 μm), the current trend is to effectively utilize NIR light in the solar spectrum for further developments of high-efficiency thin-film photovoltaic cells. For this type of photovoltaic cells, TCO electrodes with high transparency in the NIR range are required for efficient introduction of NIR light to the light-absorbing layers [1–3].

Conventional TCOs like Sn-doped In$_2$O$_3$ (ITO) and Al-doped ZnO (AZO) usually have low transparency in the NIR region because their low resistivity is obtained by maximizing the electron density (~10^{21} cm^{-3}). Such high electron density gives a typical plasma wavelength of ~1 μm and thus leads to opaqueness in the NIR region. To improve the NIR transparency, it is necessary to make the plasma wavelength longer by suppressing the electron density. In addition, the electron mobility must be simultaneously increased to retain high conductivity. In other words, it is necessary to develop high-mobility TCOs (HMTCOs) with suppressed electron density.

The development of HMTCOs would also lead to improvements in the performance of energy-efficient electrochromic (EC) windows. Thin films of TCOs are also used in EC windows as a transparent electrode [4–7]. Since conventional TCOs allow passage of only visible light in the solar spectrum, EC windows using conventional TCOs do not make use of NIR light, which accounts for nearly half of the solar

* Corresponding author.
E-mail address: n-yamada@isc.chubu.ac.jp (N. Yamada).

spectrum [8], even when the EC layers are in their transparent state. To improve the energy performance of EC windows in the winter, it is desirable for EC windows to be transparent in the entire wavelength range of the solar spectrum and simultaneously reflective against thermal radiation from a room, which peaks at a wavelength of ~10 μm [9]. This would be possible if conventional TCOs are replaced with HMTCOs.

Many studies have focused on improving the mobility of TCOs to enhance their optoelectronic performance. Ever since Meng et al. reported extraordinarily high electron mobility values of 80–130 cm^2 V^{-1} s^{-1} in Mo-doped In$_2$O$_3$ (IMO) polycrystalline films [10,11], exploration of HMTCOs has been initiated in earnest. Shortly after the first report, several other research groups confirmed that IMO is a true HMTCO [12–18]. In the early stages of the research, physical vapor deposition (PVD) techniques were exclusively used to grow IMO films. In recent years, several studies have demonstrated that some atmospheric techniques can be employed to deposit high-mobility IMO thin films [19–22]. It has been shown that In$_2$O$_3$ doped with a transition metal (W [23], Ti [24–26], or Zr [27–29]) or hydrogen [2,30,31] is also a HMTCO. Moreover, SnO$_2$-based HMTCOs have recently been reported [32–34].

Among these HMTCOs, IMO has been studied most extensively: both experimental and theoretical studies [19,35] have been reported. Mo atoms in oxides exist in various oxidation states. In IMO, the electrically active Mo is in the +4 instead of the +6 oxidation state [12,14]. When the fraction of Mo^{4+} in IMO increases, a highly conductive IMO film is obtained as a result of increases in both electron density and mobility [12]. Very recently, Bhachu et al. elucidated the origin of high electron mobility in IMO [19]. They showed that very small hybridization of the Mo^{4+} 4d and In^{3+} 5s states at the bottom of the conduction band gives rise to significantly reduced ionized-impurity scattering and thus enhanced electron mobility: the Mo^{4+} ions in IMO can be regarded as "remote" impurities [19].

Somewhat surprisingly, even though IMO has been extensively studied (as described above), there is no general knowledge of the optimum doping concentration of Mo, which is quite a contrast to the cases of ITO and AZO. While high-mobility IMO thin films have often been reported in the literature, each of these studies cited a different optimum Mo-dopant concentration in the range of 1 to 5 at%: some papers define the optimum value by the film composition, whereas others express it as the target composition [3,36]. As a result, a definitive optimum Mo-dopant concentration in high-mobility IMO is far from being established.

Optimization of thin-film composition using a batch-type PVD system is hardly an efficient technique because sintered targets with various compositions must be prepared. For high-throughput optimization of thin-film composition, a combinatorial approach in PVD has sometimes been employed [37], which is an excellent strategy, but it needs a rather expensive system and is not suitable for all users.

As an alternative, we suggest using atmospheric-pressure mist chemical-vapor deposition (mist-CVD) [38] to quickly determine the optimum composition of oxide thin films. Mist-CVD is a powerful tool for the following three reasons. The thin-film composition can be easily and widely controlled just by changing the composition of the starting solutions. In addition, mist-CVD allows us to deposit oxide thin films with various compositions in a short time without requiring expensive components because it is an atmospheric process that utilizes a simple deposition system. Furthermore, it has been demonstrated that high-quality oxide thin films can be deposited by mist-CVD technique [38–45]. Once an optimum composition is found, PVD is used to prepare oxide thin films with this composition. Therefore, the combination of mist-CVD and PVD is another method for high-throughput synthesis and screening of functional oxide thin films.

Among various PVD techniques, sputtering is widely used in industry to deposit TCO thin films. Thus, we addressed the optimization of IMO thin films by combining mist-CVD with sputtering. We found the optimum Mo-dopant concentration in a short time by using mist-CVD, and then we applied the optimum Mo-dopant concentration to

sputter-deposition of IMO thin films. Consequently, sputtered IMO thin films with excellent optical and electrical properties were successfully obtained. In the following sections, we will demonstrate that the combination of mist-CVD and sputtering offers an effective way to optimize IMO thin films.

2. Experiments

2.1. Thin-film deposition

IMO thin films were deposited by the mist-CVD method. We built a mist-CVD system according to a design reported in the literature [38]. A 0.1 M solution of InCl$_3$·4H$_2$O (purity 99.9%) in absolute methanol was used as the starting solution. For Mo-doping, MoCl$_5$ (purity 99.5%) was added to the starting solution so that the Mo concentration in the solution was in the range of 0–10 at%. Prior to the deposition runs, the starting solutions were vigorously stirred for an hour and then we visually checked that the solutes (InCl$_3$·4H$_2$O and MoCl$_5$) were fully dissolved. The solutions were ultrasonically atomized using an ultrasonic oscillator with an oscillating frequency of 2.4 MHz (Honda Electronics HM-2412). The misted vapor was transported to the substrate (Corning Eagle XG) through a linear nozzle using N$_2$ as the carrier gas at a flow rate of 1.0 L min^{-1}. A glass substrate with an area of 10 × 10 mm^2 was placed on a hot plate and heated at 400 °C. The temperature of the substrate surface during the deposition was monitored using a K-type thermocouple. The deposition time was at 1 min to deposit thin films with a thickness in the range of 150–250 nm. The as-deposited films were subsequently annealed in vacuum (3 × 10^{-3} Pa) at 600 °C for 1 h using a lamp annealing system (ULVAC-RIKO MILA-5000).

We also deposited IMO thin films by radio-frequency (RF) magnetron sputtering. All the depositions were performed on glass substrates heated at 100–500 °C. We used a disk (diameter: 10 cm) consisting of a hot-pressed mixture of In$_2$O$_3$ and Mo metal as the target. The target was purchased from Toshima Manufacturing Co., Ltd. The atomic percent of Mo in the target, $(N_{Mo}/N_{In+Mo}) \times 100\%$, was 1.0 at%, which was determined by inductively coupled plasma atomic emission spectroscopy (ICP–AES; Seiko SPS-3000). From powder X-ray diffraction (XRD) measurements (Rigaku RINT-TTR II), we confirmed that the target was the cubic In$_2$O$_3$ phase. No impurity phase, including Mo metal, MoO$_2$, and MoO$_3$, was observed. In other words, we used a phase-pure IMO target. Sputtering was conducted under an Ar (99.999% pure) atmosphere at a total pressure of 0.3 Pa. An RF power of 100 W was applied to the IMO target. The deposition time was 30 min, and the typical thickness of the thin films was approximately 500 nm. The thicknesses of the films were evaluated by using X-ray reflectivity (XRR) measurements for 2θ ranging from 0 to 1.0°, by using the same diffractometer with XRD. From the period of the Kiessing fringes in the XRR spectra, the thicknesses of the films were extracted [46].

2.2. Characterization

The crystalline phase of the films was examined by XRD, using a diffractometer with Cu K$_\alpha$ radiation (Rigaku ATX-G). The surface morphology of the films was observed with a scanning electron microscope (SEM; JEOL JSM-6510 LA). The film composition, represented by the atomic percent of Mo, was determined by inductively coupled plasma atomic emission spectroscopy (ICP–AES; Shimadzu ICPE-9810). X-ray photoelectron spectroscopy (XPS) using monochromated Al K$_\alpha$ radiation (ULVAC-PHI Versa Probe) was employed for examining the chemical state of Mo in IMO films. The XPS measurements were performed on both as-deposited and on 10-min-Ar$^+$-sputtered surfaces. The sputter-etching was carried out by using an argon-ion gun with an ion energy of 4 keV, an emission current of 7 mA, and a raster size of 3 mm × 3 mm. The etching rate was roughly 3 nm/min.

The electrical resistivity was measured at room temperature (RT) using the van der Pauw method with a source current of 1 mA. The

electron density and mobility were determined at RT by Hall effect measurements in the van der Pauw configuration (Toyo Corp. Resistest 8200) with a source current of 1 mA. Magnetic fields of $+1$ and -1 T were applied normal to the film surface. The optical transmittance and reflectance in the ultraviolet to near-infrared region were measured using a spectrometer (Shimadzu UV-3150). We also measured the infrared transmittance and reflectance using a Fourier-transform infrared (FTIR) spectrometer (Shimadzu IRAffinity-1).

3. Results and discussion

3.1. IMO thin films deposited by mist-CVD

Fig. 1 shows the film composition (indicated by the atomic percent of Mo) as a function of the composition of the starting solution. The film compositions were determined by using inductively coupled plasma atomic emission spectroscopy (ICP-AES). We made the calibration curves of the intensity of the emission from In (the wavelength of 230.61 nm) and Mo (the wavelength of 202.03 nm) using the standard solutions with various Mo/In ratios to determine the film composition. As shown in Fig. 1, the film composition linearly changed with the solution composition, and the Mo content in the film was always lower than that in the solution. The approximate straight line in Fig. 1 shows that the film composition was approximately 39% of the solution composition. Similar phenomenon was also reported by Sawada et al. for spray pyrolytic ITO films [49]. The reason why the Mo concentrations in the films were always lower than those in the starting solutions has not been clarified yet. At present, we speculate that undissolved $MoCl_5$ remained in the starting solutions because $MoCl_5$ dissolves slowly in methanol. Although the visual check of the starting solutions suggested the complete dissolution of $MoCl_5$, undissolved $MoCl_5$ maybe remained still in the starting solutions (we could not find the literature data of the solubility limit in methanol). The particles of the undissolved $MoCl_5$ is not expected to be carried by the mist from the starting solutions to the substrate surface. Thus, we think that the lower molybdenum concentrations in the films were resulted from the existence of the unresolved $MoCl_5$ in the starting solutions.

Fig. 2(a) shows θ–2θ X-ray diffraction (XRD) patterns of the as-deposited IMO films, which indicate that all the films were polycrystalline. All the diffraction peaks can be assigned to the cubic In_2O_3 phase, indicating that $InCl_3$ reacted with oxygen in the air and thoroughly converted to In_2O_3 on the substrate surface. No secondary phase, including MoO_3 and MoO_2, was detected, implying that Mo was incorporated in In_2O_3. There are two possible oxygen sources in the air for the formation of IMO thin films from $InCl_3$ and $MoCl_5$ on the substrate surface: one is O_2 gas and the other is the water vapor. When the molar fraction of $MoCl_5$ in the solute is represented as x, the chemical reaction of $InCl_3$

Fig. 2. (a) X-ray diffraction (XRD) patterns of as-deposited IMO films with Mo concentrations of 0, 0.7, 1.5, 2.3, and 3.1 at%. Standard powder XRD patterns of (a) In_2O_3 [51], (b) MoO_3 [52], and (c) MoO_2 [53]. Peaks marked by asterisks are diffraction lines from the sample holder.

and $MoCl_5$ with O_2 can be written as,

$$2(1-x)InCl + 2xMoCl_5 + \frac{2}{3}O_2 \rightarrow In_{2(1-x)}Mo_{2x}O_3 + (2x+3)Cl_2\ (g) \quad (1)$$

On the other hand, when the water vapor in the air serves as the oxygen source, the chemical reaction can be expressed as below.

$$2(1-x)InCl + 2xMoCl_5 + (3+2x)H_2O\ (g) \rightarrow In_{2(1-x)}Mo_{2x}O_3$$
$$+ (4x+6)HCl_2\ (g) + x\,O_2\ (g) \quad (2)$$

We speculate that both the chemical reactions occurred on the substrate surface.

A typical scanning electron microscope (SEM) image at 30,000× magnification of the surface of an IMO film is displayed in Fig. 3. Such surface morphology is commonly seen in In_2O_3-based polycrystalline films deposited by similar techniques, including spray CVD [22,50] and aerosol-assisted CVD [19]. As shown in this figure, the IMO films obtained in this study were composed of crystalline grains with diameters of approximately 100 nm, and they were densely and uniformly packed together. To check the presence of residual chlorine, X-ray
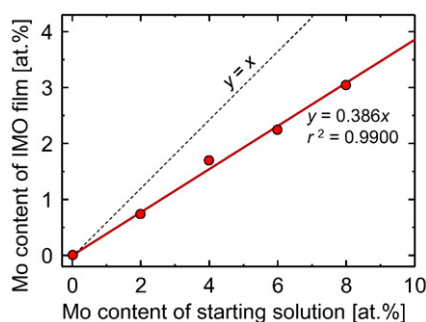

Fig. 1. Composition of Mo-doped indium oxide (IMO) film (represented by the atomic percent of Mo) as a function of composition of the starting solution (represented by the atomic percent of Mo). The dashed line indicates the ideal case when the film composition is equivalent to the solution composition.
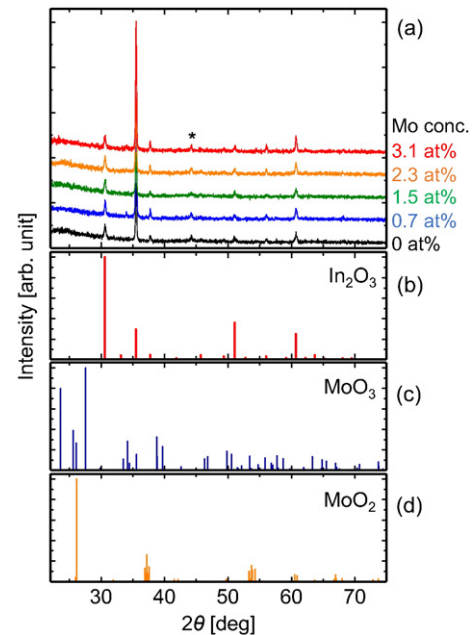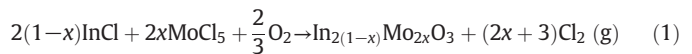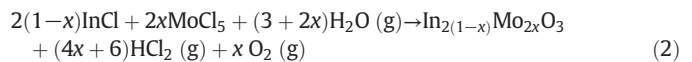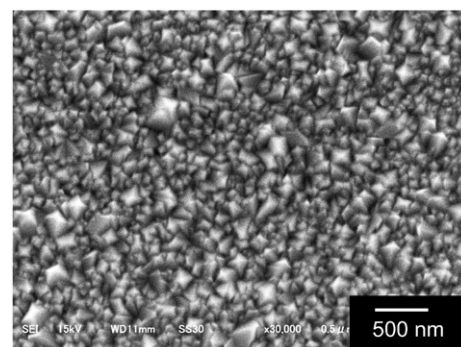

**Fig. 3.** Typical top-view scanning electron microscope (SEM) image of an as-deposited IMO film.

photoemission spectroscopy measurement (XPS) was employed. The Cl 2p line (the binding energies of $InCl_3$ and $MoCl_5$ were reported to be 199.0 and 199.8 eV [47,48], respectively) was not observed on the film surface and sputter-etched surface (the depth was roughly 30 nm), indicating that the chlorine content was below the detection limit of XPS.

As mentioned in section 1, the oxidation state of Mo in In_2O_3 is a key factor to achieving high mobility. We examined the oxidation state of Mo in IMO films by measuring the XPS Mo 3d core spectra. Fig. 4(a) shows the Mo 3d core spectrum of an as-deposited film doped with 2.3 at% Mo. The spectrum is composed of two doublets: the higher binding energy (BE) component located at BE = 232.7 eV is assigned to Mo^{6+}, while the lower BE component at BE = 231.3 eV is attributed to Mo^{4+} [19]. These assignments are reasonable because Mo^{6+} and Mo^{4+} peaks from oxides usually appear at the binding energies of 232.5–233.0 eV and 231.0–232.0 eV [54–59], respectively. From the integrated intensity ratio of these doublets, the $[Mo^{4+}]/[Mo^{6+}]$ ratio was estimated to be 1.18, that is, 54% of Mo in the as-deposited film was in the electrically active +4 oxidation state. Since it has been reported that vacuum annealing can effectively increase the fraction of Mo^{4+} [16], the as-deposited films were annealed in vacuum (3×10^{-3} Pa) at 600 °C for 1 h. As shown in Fig. 4(b), 89% of Mo in the annealed film was in the +4 oxidation state, which means that vacuum annealing increased the fraction of Mo^{4+} by a factor of 1.6.

It has been known that the main electron donor in IMO is Mo^{4+} rather than Mo^{6+} [12,14], even though Mo^{6+} at indium sites in In_2O_3 is expected to be a three-electron donor. It has also been postulated that Mo^{6+} will be compensated by interstitial oxygen to form a neutral defect complex, which is expressed using the Kröger–Vink notation [60] as $(2Mo_{In}^{\cdots}3O_i'')^x$. Since the IMO films in the present study were deposited under atmospheric conditions, it was likely that interstitial oxygen was incorporated. Thus, we think that the Mo^{6+} peaks in Fig. 3(a) and (b) correspond to the neutral $(2Mo_{In}^{\cdots}3O_i'')^x$ complex. On the other hand, the Mo^{4+} peaks in Fig. 4 correspond to substitutional tetravalent Mo^{4+}, which served as a one-electron donor ($Mo_{In}^{\bullet} + e'$). The higher concentration of the Mo^{4+} component in the annealed film suggests that the neutral defect complex dissociated upon vacuum annealing in

accordance with the following reaction [14]:

$$\left(2Mo_{In}^{\cdots}3O_i''\right)^x \rightarrow 2Mo_{In}^{\bullet} + 2e' + \frac{3}{2}O_2(g) \tag{3}$$
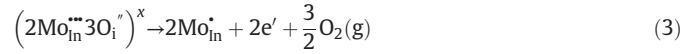
In other words, vacuum annealing resulted in an increase in conduction electron density, which was confirmed by the Hall-effect measurements, as discussed below.

The dependence of the electron density (n_e) on Mo concentration in the as-deposited and annealed films is presented in Fig. 5(a). The value of n_e increased as the Mo concentration increased and reached a plateau at a Mo concentration of ~2 at% for both as-deposited and annealed films. From these results, the upper limit of Mo-doping was roughly estimated to be 2 at%. The n_e values of the annealed films were approximately 1.5 times as large as those of the as-deposited films, which is reasonably consistent with the increase in the fraction of the Mo^{4+} component by the dissociation of the neutral $(2Mo_{In}^{\cdots}3O_i'')^x$ complex upon vacuum annealing. When the Mo content was <1 at%, the experimental n_e values reasonably agreed with the theoretical line calculated by assuming that each Mo atom in IMO released one electron.

As for the IMO thin films with the Mo concentrations higher than 2 at%, the n_e values were always lower than the theoretical values. For example, the as-deposited IMO film doped with 2.3 at% Mo had the experimental n_e value of 3.6×10^{20} cm^{-3}, whereas the theoretical n_e value on the dashed line in Fig. 5(a) for this film was 7.1×10^{20} cm^{-3}. The theoretical n_e values in Fig. 5(a) were calculated based on the assumption that all the Mo atoms in IMO released one electron. However, as discussed above, the analysis of Mo 3d core spectrum of this film suggested that only 54% of the Mo atoms in the IMO film was in +4 state. This means that the Mo^{4+} concentration in this film was 1.2 at%. From this concentration, the n_e value was estimated to be 3.8×10^{20} cm^{-3},
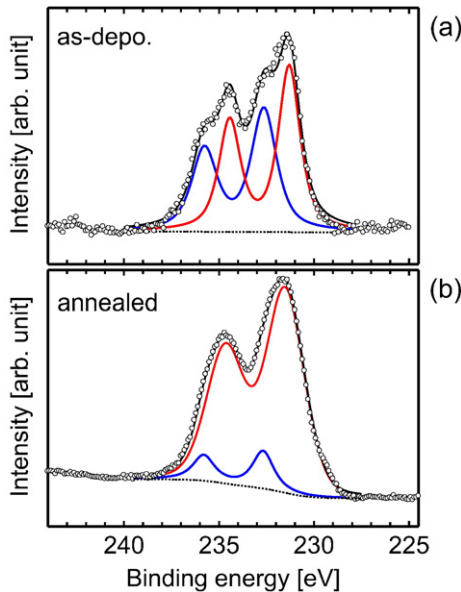
Fig. 4. Mo 3d core spectra obtained by X-ray photoelectron spectroscopy (XPS) for (a) as-deposited and (b) vacuum-annealed films doped with 2.3 at% Mo. The open circles represent experimental data points, the solid lines are best fits to the data, and the dotted lines represent the background signals. The red and blue solid lines are designated as Mo^{4+} and Mo^{6+}, respectively.
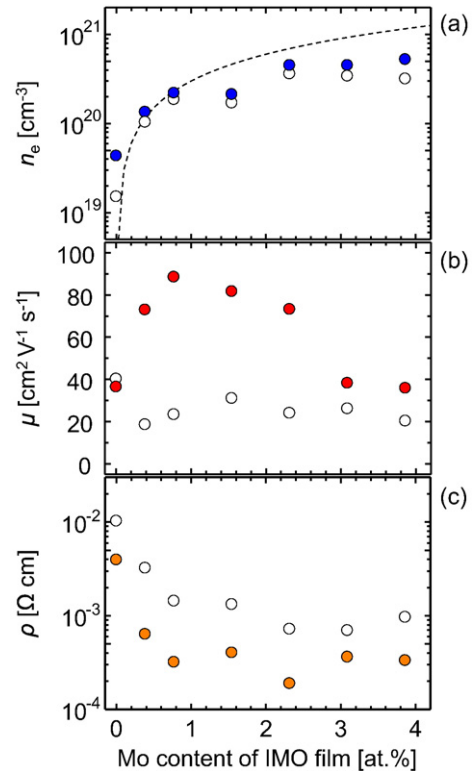
Fig. 5. Mo-concentration dependence of the (a) electron density (n_e), (b) mobility (μ), and (c) resistivity (ρ) of prepared IMO films. The open circles represent data points of the as-deposited films, and the solid circles represent data points of the annealed films. The dashed curve in the top panel shows the calculated electron density based on the assumption that each Mo atom in IMO released one electron.

which agrees well with the experimental n_e value. In the case of the annealed film with the Mo doping concentration of 2.3 at.%, the n_e value determined by Hall-effect measurement was 5.0×10^{20} cm^{-3}. Since 89% of the Mo atoms in this film was in +4 state, the Mo^{4+} concentration was calculated to be 2.0 at.%. Using this concentration, the n_e value was estimated to be 6.3×10^{20} cm^{-3}, which roughly agrees with the n_e value determined by Hall-effect measurement. We believe that these results support the hypothesis that the main electron donor in IMO is Mo^{4+} rather than Mo^{6+}.

The electron mobility (μ) is plotted as a function of the Mo content in Fig. 5(b). For the as-deposited films, the μ values were in the range of 20–30 cm^2 V^{-1} s^{-1} regardless of the Mo content. The μ values for IMO films with Mo-dopant concentration below the doping limit (~2 at%) showed remarkable increases upon vacuum annealing. Notably, μ values above 80 cm^2 V^{-1} s^{-1} were obtained at Mo concentrations of 0.8–1.6 at.% The maximum μ value of 89 cm^2 V^{-1} s^{-1} was obtained for the film with Mo content of 0.8 at%. The substantial increase in μ upon vacuum annealing was probably due to the decomposition of the $(2Mo_{In}^{\cdots}3O_i'')^x$ complex defects. The $(2Mo_{In}^{\cdots}3O_i'')^x$ complex defects were expected to behave as electron scattering centers because the $(2Sn_{In}^{\bullet}O_i'')^x$ complex defects in ITO have been known to act as scattering centers with a scattering cross section of $(4–8) \times 10^{-16}$ cm^2 [61,62]. If the complex defects dissociated upon vacuum annealing in accordance with Eq. (3), the defect would have turned into the "remote" impurity, thus significantly increasing the electron mobility.

Fig. 5(c) depicts the dependence of the film resistivity (ρ) on Mo content. The annealed films containing ≥0.8 at% Mo exhibited low ρ values of $(2–3) \times 10^{-4}$ Ω cm, which were nearly constant for all Mo concentrations. For the annealed films containing <2 at% Mo, low ρ values were obtained even though these films had relatively small n_e values of ~2×10^{20} cm^{-3}. In other words, the low ρ values were mainly attributable to high μ values. In contrast, large n_e values of ~5×10^{20} cm^{-3} were a major cause of the low ρ values for the annealed films with higher dopant concentrations. From the view point of NIR transparency, n_e should be kept as low as possible without sacrificing electrical conductivity. Hence, a Mo concentration of ~1 at% is preferable for achieving both low ρ and high NIR transmittance.

Indeed, as shown in Fig. 6, an annealed IMO film doped with 0.8 at% Mo exhibited high transmittance (>75%) over a wide wavelength range of 0.4–2.5 μm even though the ρ value of this film was as low as 3.2×10^{-4} Ω cm. This IMO film had $n_e = 2.2 \times 10^{20}$ cm^{-3}, and thus its plasma wavelength (λ_p) was estimated to be 3.7 μm from the

equation

$$\lambda_p = \sqrt{\frac{\varepsilon_0 \varepsilon_\infty m^*}{e n_e}},\qquad(4)$$

where $\varepsilon_0, \varepsilon_\infty, c, m^*$, and e denote the dielectric constant of vacuum, high-frequency permittivity, speed of light, effective mass, and elementary charge, respectively. In the estimation, we used $m^* = 0.3\, m_0$ (m_0 is the free electron mass) and $\varepsilon_\infty = 9$ [63]. The high transparency in the wide range of wavelengths is ascribed to the long λ_p. The results of both electrical and optical measurements led us to the conclusion that a Mo concentration of ~1 at% is the optimum dopant concentration for highly conductive IMO thin films with good NIR transparency.

3.2. Sputter-deposition of IMO films with the optimum composition

Next, we adopted the optimum composition for sputter-deposition of IMO thin films. More specifically, we used an IMO target with the optimum Mo concentration of 1 at% for the deposition processes. To minimize the formation of $(2Mo_{In}^{\cdots}3O_i'')^x$, the deposition was carried out without introducing oxygen gas into the deposition chamber. IMO thin films were deposited on glass substrates at three deposition temperatures of 100, 300, and 500 °C. The Mo content in the as-deposited films was in a range of 1.3–1.7 at% and hardly depended on the deposition temperature (T_d).

Fig. 7 shows n_e and μ values of sputtered IMO thin films as functions of T_d. While μ exhibited strong T_d dependence, the T_d dependence of n_e was relatively weak. The IMO thin films deposited at $T_d = 100–300$ °C had μ values of ~30 cm^2 V^{-1} s^{-1}, which are similar to typical μ values of sputtered ITO thin films. When T_d was increased to 500 °C, a steep increase in μ occurred, reaching 93 cm^2 V^{-1} s^{-1} at $T_d = 500$ °C. As a result, a highly conductive IMO film with $\rho = 4.4 \times 10^{-4}$ Ω cm was obtained at $T_d = 500$ °C. The results of the mist-CVD experiments assisted us in obtaining the high-mobility IMO film in only three sputter-deposition runs without any post-deposition treatment, suggesting that the combination of mist-CVD and sputtering is an effective way to rapidly optimize the composition of oxide thin films.

As discussed above, the electron transport properties of IMO films are closely related to the oxidation state of Mo in IMO. We carried out XPS measurements of Mo 3d core spectra for the sputtered thin films to examine the oxidation state. Mo 3d core spectra for the IMO films deposited at $T_d = 100, 300,$ and 500 °C are shown in Fig. 8(a), (b), and (c), respectively. For the IMO films deposited at $T_d = 100$ and 300 °C, more than half of the Mo in the IMO films was in the +6 oxidation state (BE ≈ 232.5 eV), as shown in Fig. 8(a) and (b). The binding energy of Mo^{6+} peak has been reported to be in the range of 232.5–233.0 eV [55,56,58,59]. Thus, $(2Mo_{In}^{\cdots}3O_i'')^x$ complex defects are considered to be present at a significant level, which led to the low μ values of
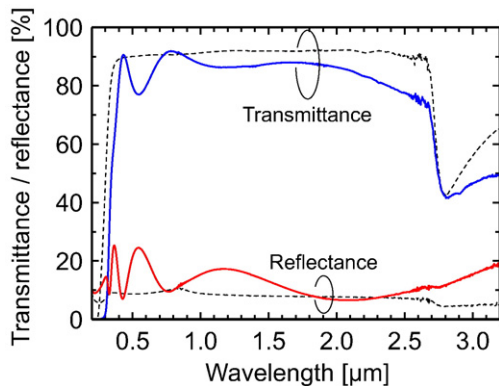
Fig. 6. Optical transmittance (blue solid line) and reflectance (red solid line) spectra of an annealed IMO film doped with 0.8 at% Mo. The IMO film had a resistivity of 3.2×10^{-4} Ω cm, an electron density of 2.2×10^{20} cm^{-3}, and an electron mobility of 89 cm^2 V^{-1} s^{-1}. The broken lines represent the spectra of the substrate.
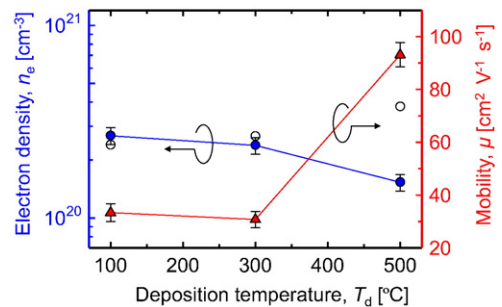
Fig. 7. Deposition temperature (T_d) dependence of electron density (n_e; circles) and mobility (μ; triangles) of sputtered IMO thin films. The closed circles represent n_e values determined by Hall-effect measurements and the open circles denote n_e values estimated using Mo^{4+} concentration in the films.
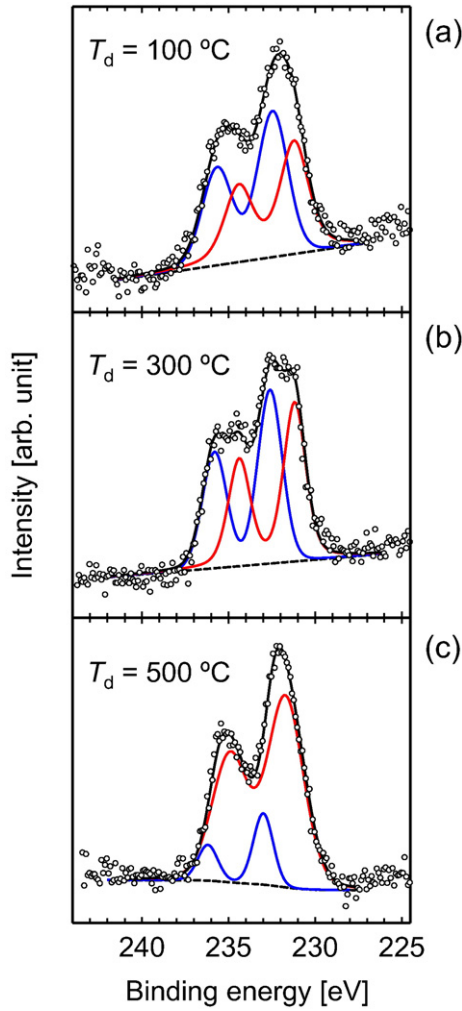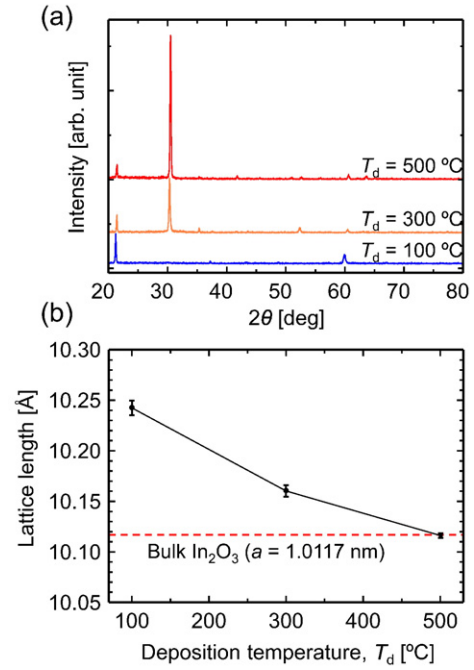
Fig. 8. Mo 3d X-ray photoemission core spectra of sputtered IMO thin films deposited at T_d = (a) 100, (b) 300, and (c) 500 °C. The open circles represent experimental data points, the solid lines are best fits to the data, and the dotted lines represent the background. The red and blue solid lines are designated as Mo^{4+} and Mo^{6+}, respectively.


Fig. 9. (a) X-ray diffraction (XRD) patterns of IMO thin films sputtered at T_d = 100, 300, and 500 °C. (b) Deposition temperature dependence of lattice length of sputtered IMO thin films.

~30 $cm^2 V^{-1} s^{-1}$. When T_d was increased to 500 °C, the Mo^{6+} component showed a substantial decrease, as shown in Fig. 8(c). Approximately 85% of Mo in the IMO film deposited at T_d = 500 °C was in the +4 oxidation state (BE ≈ 231.5 eV). Mo^{4+} peak from oxides generally appears at binding energies ranging from 231.0 to 232.0 eV [54–57]. According to the Mo–O phase diagram [64], the +4 oxidation state is more stable than the +6 state at high temperature. Thus, the deposition at 500 °C under an oxygen-poor atmosphere probably suppressed the formation of the $(2Mo_{In}^{\cdots} 3O_i^{''})^x$ complex defects. Consequently, μ of the IMO film deposited at 500 °C reached the high value of 93 $cm^2 V^{-1} s^{-1}$. These results indicate that the variation in $[Mo^{4+}]/[Mo^{6+}]$ ratio with increasing T_d was one reason for the T_d dependence of μ shown in Fig. 7.

Fig. 9(a) shows θ–2θ XRD patterns of the IMO thin films. The diffraction peaks sharply intensified when T_d was increased to 500 °C, indicating that the crystallinity improved. Thus, we think that the improvement in crystallinity was an additional reason for the high μ value of the IMO film deposited at T_d = 500 °C.

It is worth noting that the diffraction peaks gradually shifted toward higher 2θ angles with increasing T_d, as shown in Fig. 9(a). The lattice length as a function of T_d is displayed in Fig. 9(b); the lattice length monotonically decreased from 10.242 ± 0.007 to 10.116 ± 0.002 Å as T_d was increased from 100 to 500 °C. This means that the lattice length

of the IMO thin films approached the bulk value (a = 10.117 Å for bulk In_2O_3), implying that strain relaxation occurred. The decrease in the lattice length (i.e., lattice strain) with increasing T_d suggests a decrease in the concentration of the $(2Mo_{In}^{\cdots} 3O_i^{''})^x$ complex in the IMO films, because of the following reasons. The $(2Mo_{In}^{\cdots} 3O_i^{''})^x$ complex is composed of the substitutional Mo (Mo_{In}) and interstitial oxygen ($O_i^{''}$). The ionic radius of oxygen is so large that the incorporation of the interstitial oxygen induces the expansion of the host lattice and thus lattice strain. On the other hand, when the $(2Mo_{In}^{\cdots} 3O_i^{''})^x$ complex decomposes, the interstitial oxygen is removed from the host lattice. The removal of the interstitial oxygen relaxes the lattice strain and decrease the lattice length. Such phenomena were already reported in literature [65]. Therefore, the decrease in the lattice length is considered to be a result of the decrease in the concentration of the complex. Namely, the variations in lattice length supports our hypothesis that the $(2Mo_{In}^{\cdots} 3O_i^{''})^x$ defects decomposed during the deposition process at T_d = 500 °C.

Here, we briefly discuss T_d dependence of electron concentration. As with the case of the mist-CVD IMO films, we estimated n_e values from the Mo^{4+} concentrations in the sputtered IMO films. The Mo^{4+} concentrations in the IMO films deposited at T_d = 100, 300, and 500 °C were calculated to be 0.77, 0.85, and 1.4 at%, respectively, from the analyses of the XPS Mo 3d core spectra shown in Fig. 8(a)–(c). The n_e values estimated using the Mo^{4+} concentrations are plotted in Fig. 7 (open circles). The estimated n_e values for the IMO films deposited at 100 and 300 °C showed good agreement with those determined by Hall-effect measurements. However, for the IMO film deposited at 500 °C, the estimated n_e value was three times as large as the n_e value determined by Hall-effect measurement. This discrepancy indicates that a large portion of the Mo^{4+} atoms in the film did not release electrons. The reason for this remains unclear yet. Further study on the chemical state of Mo in IMO thin films is still needed to reveal the reason.

Finally, the optical properties of the sputtered IMO film with ρ = $4.4 \times 10^{-4} \Omega$ cm and μ = 93 $cm^2 V^{-1} s^{-1}$ were examined. This IMO film had a thickness of 550 nm, so that the sheet resistance was as low as 8 Ω sq^{-1}. The transmittance and reflectance spectra in the ultraviolet to infrared wavelength (λ) range are depicted in Fig. 10(a). The IMO film had high transmittance in the visible and NIR region: light transmittance of ~55% was maintained even at a wavelength of 2.5 μm. The
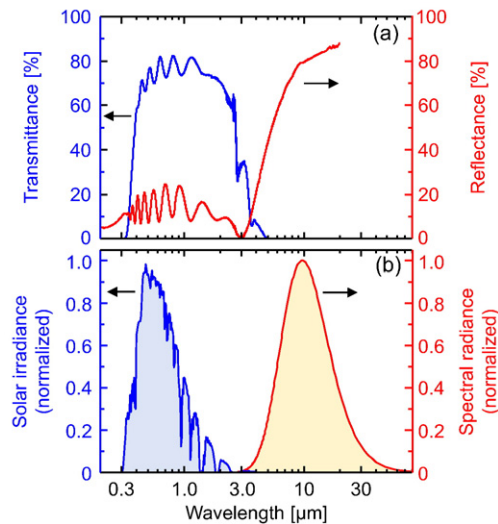
Fig. 10. (a) Optical transmittance and reflectance spectra of an IMO thin film with an electron density of 1.5×10^{20} cm^{-3} and mobility of 93 cm^2 V^{-1} s^{-1}. (b) Normalized air-mass 1.5 solar spectrum and thermal radiation spectrum at 293 K. The thermal radiation spectrum was calculated using Planck's law.

plasma wavelength was estimated to be longer than 4 μm for this film, which accounts for such a wide transmittance window. As shown in Fig. 10(b), the air-mass 1.5 solar spectrum mostly spans a range of $\lambda = 0.3$–2.5 μm, indicating that the IMO film was transparent in almost the entire wavelength range of the solar spectrum.

Fig. 10(b) shows the thermal radiation spectrum calculated from Planck's law [66] by assuming a temperature of 293 K is shown in Fig. 10(b). The spectrum rises at $\lambda \approx 3$ μm, and its peak is in the vicinity of $\lambda \approx 10$ μm. As shown in Fig. 10(a), the reflectance spectrum of the IMO film also shows a steep increase at $\lambda \approx 3$ μm. The reflectance reached ~80% at a wavelength of 10 μm. This behavior of the reflectance can be understood in the framework of the free-electron model. The steep increase in the reflectance stemmed from the high electron

mobility, which means that the IMO film effectively reflected the thermal radiation at room temperature.

As described above, the optimized IMO films in this study allowed passage of the full solar spectrum and reflected only light corresponding to thermal radiation at room temperature. Therefore, the optimized IMO films are applicable not only to transparent electrodes in photovoltaic cells, but also to heat-reflective electrodes in energy-efficient EC windows.

3.3. Comparison of electron transport properties

In this section, we compare the electrical properties of IMO thin films deposited by various techniques. Table 1 summarizes the electrical properties of IMO polycrystalline films deposited by atmospheric processes and sputtering. IMO thin films usually show high μ values, which are roughly 2–3 times higher than typical values for ITO films (30–50 cm^2 V^{-1} s^{-1}), regardless of the deposition process. It is noteworthy that mobility values higher than 90 cm^2 V^{-1} s^{-1} have generally been obtained at the Mo concentrations near 1 at% [16,19,20,36]. This fact supports our conclusion that the Mo doping concentration of ~1 at% is optimum.

For IMO films deposited by atmospheric process, μ values higher than 100 cm^2 V^{-1} s^{-1} have been frequently reported. However, the μ values of mist-CVD IMO films in this study did not exceed 100 cm^2 V^{-1} s^{-1}. The main aim of the mist-CVD experiments in this study was to examine the optimum Mo-doping concentration. Thus, we did not optimize the growth condition in detail. We expect that further optimization of the growth condition leads to enhancement of electron mobility. The sputtered IMO thin film in the present study has one of the highest μ values among the sputtered IMO films. Since the past studies of the sputtered IMO thin films used targets with the Mo concentration of 3–4 wt% (4–6 at%), which are higher than the optimal concentration, somewhat low μ values were probably obtained. The key to achieving high electron mobility in this study was the use of the target with the optimum Mo concentration, which was determined from the mist-CVD experiments. We believe that this achievement of high μ in sputtered IMO films is highly significant, because sputtering is commonly used in industry to deposit TCO thin films.

Table 1
Comparison of electrical properties of IMO polycrystalline films deposited by various techniques.

Technique	Mo concentration	T_d [°C]	ρ [Ω cm]	n_e [cm^{-3}]	μ	Ref.
[cm^2 V^{-1} s^{-1}]						
Mist-CVD (atmospheric process)	0.7 at%	400*	3.2×10^{-4}	2.2×10^{20}	89	This study
AA-CVD (atmospheric process)	1 mol%[†]	450	1.2×10^{-4}	4.4×10^{20}	119	[19]
Spray pyrolysis (atmospheric process)	0.5 at%	400*	4.0×10^{-4}	1.0×10^{20}	149	[36]
Spray pyrolysis (atmospheric process)	0.5 at%	400	1.8×10^{-3}	4.6×10^{19}	77	[20]
Spray pyrolysis (atmospheric process)	6 at%[†]	400	7.3×10^{-4}	5.0×10^{20}	34	[67]
RF sputtering (vacuum process)	1.3 at%	500	4.4×10^{-4}	1.5×10^{20}	93	This study
RF sputtering (vacuum process)	4 wt%[‡]	350	1.1×10^{-3}	1.3×10^{20}	44	[12]
RF sputtering (vacuum process)	4 wt%[‡]	450	2.5×10^{-4}	3.0×10^{20}	83	[13]
RF co-sputtering (vacuum)	2.0 at%	450*	2.3×10^{-4}	2.7×10^{20}	99	[16]
DC sputtering (vacuum)	3 wt%[‡]	350	3.7×10^{-4}	4.0×10^{20}	42	[68]

T_d – Deposition temperature; ρ – resistivity; n_e – electron density; μ – electron mobility; AA-CVD – aerosol-assisted chemical vapor deposition.
[†] Composition of the starting solution.
[‡] Composition of the target.
* Postdeposition annealed in vacuum.

4. Conclusion

Rapid optimization of high-mobility IMO thin films with excellent transparency in the NIR region was conducted by a combination of mist-CVD and sputtering. The use of mist-CVD enabled us to deposit IMO thin films with various Mo-dopant concentrations in a short period of time. Electrical evaluations and chemical analyses of these films revealed that the optimum Mo-dopant concentration was 1 at% and the oxidation state of Mo in IMO should be +4 to achieve high mobility. The optimized film showed high optical transmittance in the wavelength range of 0.3–2.5 µm even though the film was highly conductive. Taking advantage of these findings, we succeeded in sputter-deposition of high-mobility IMO thin films in only a few rounds of experiments. As a result, a highly conductive IMO film with a high electron mobility of 93 cm^2 V^{-1} s^{-1} and relatively low electron density of 1.5×10^{20} cm^{-3} was attained. Since the IMO film had a plasma wavelength longer than 4 µm, it allowed passage of the full solar spectrum and effectively reflected only far-infrared light corresponding to thermal radiation at room temperature. Therefore, optimized IMO films are applicable not only to transparent electrodes in photovoltaic cells, but also to heat-reflective electrodes in energy-efficient EC windows. These results indicate that the combination of mist-CVD and sputtering is a low cost and efficient way to optimize the composition of IMO thin films with excellent electrical and optical properties. We believe this combination can be extended to optimization of other functional oxide systems.

Acknowledgments

References

[1] S. Calnan, H.M. Uphadhyaya, S. Buecheler, G. Khrypunov, A. Chirila, A. Romeo, R. Hashimoto, T. Nakada, A.N. Tiwari, Application of high mobility transparent conductors to enhance long wavelength transparency of the intermediate solar cell in multi-junction solar cells, Thin Solid Films 517 (2009) 2340–2343.
[2] T. Koida, H. Fujiwara, M. Kondo, High-mobility hydrogen-doped In$_2$O$_3$ transparent conductive oxide for a-si:h/c-si heterojunction solar cells, Sol. Energy Mater. Sol. Cells 93 (2009) 851–854.
[3] S. Calnan, A.N. Tiwari, High mobility transparent conducting oxides for thin film solar cells, Thin Solid Films 518 (2010) 1839–1849.
[4] D.S. Ginley, H. Hosono, D.C. Paine, Handbook of Transparent Conductors, Springer, New York, 2010.
[5] C. Drososa, D. Vernardou, Perspectives of energy materials grown by APCVD, Sol. Energy Mater. Sol. Cells 140 (2015) 1–8.
[6] K. Psifis, D. Louloudakis, D. Vernardou, E. Spanakis, G. Papadimitropoulos, D. Davazoglou, N. Katsarakis, E. Koudoumas, Effect of O$_2$ flow rate on the electrochromic response of WO$_3$ grown by LPCVD, Phys. Status Solidi C 12 (2015) 1011–1015.
[7] D. Vernardou, K. Psifis, D. Louloudakis, G. Papadimitropoulos, D. Davazoglou, N. Katsarakis, E. Koudoumas, Low pressure CVD of electrochromic WO$_3$ at 400 °C, J. Electrochem. Soc. 162 (2015) H579–H582.
[8] C.G. Granqvist, Materials Science for Solar Energy Conversion Systems, Pergamon Press, Oxford, 1991.
[9] K. Yoshimura, Direction dependence of savings on cooling and heating loads by energy efficient windows, J. Energy Power Eng. 8 (2014) 2012–2016.
[10] Y. Meng, X. Yang, H. Chen, J. Shen, Y. Jiang, Z. Zhang, Z. Hua, A new transparent conductive thin film In$_2$O$_3$:Mo, Thin Solid Films 394 (2001) 218–223.
[11] Y. Meng, X. Yang, H. Chen, J. Shen, Y. Jiang, Z. Zhang, Z. Hua, Molybdenum-doped indium oxide transparent conductive thin films, J. Vac. Sci. Technol. A 20 (2002) 288–293.
[12] Y. Yoshida, T.A. Gessert, C.L. Perkins, T.J. Coutts, Development of radio-frequency magnetron sputtered indium molybdenum oxide, J. Vac. Sci. Technol. A 21 (2003) 1092–1097.
[13] Y. Yoshida, D.M. Wood, T.A. Gessert, T.J. Coutts, High-mobility, sputtered films of indium oxide doped with molybdenum, Appl. Phys. Lett. 84 (2004) 2097–2099.
[14] C. Warmsingh, Y. Yoshida, D.W. Readey, C.W. Teplin, J.D. Perkins, P.A. Parilla, L.M. Gedvilas, B.M. Keyes, D.S. Ginley, High-mobility transparent conducting Mo-doped In$_2$O$_3$ thin films by pulsed laser deposition, J. Appl. Phys. 95 (2004) 3831–3833.
[15] A.E. Delahoy, S.Y. Guo, Transparent and semitransparent conducting film deposition by reactive-environment, hollow cathode sputtering, J. Vac. Sci. Technol. A 23 (2005) 1215–1220.
[16] N. Yamada, T. Tatejima, H. Ishizaki, T. Nakada, Effects of postdeposition annealing on electrical properties of Mo-doped indium oxide (IMO) thin films deposited by RF magnetron cosputtering, Jpn. J. Appl. Phys. 45 (2006) L1179–L1182.
[17] M.F.A.M. van Hest, M.S. Dabney, J.D. Perkins, D.S. Ginley, High-mobility molybdenum doped indium oxide, Thin Solid Films 496 (2006) 70–74.
[18] R.K. Gupta, K. Ghosh, S.R. Mishra, P.K. Kahol, Structural, optical and electrical characterization of highly conducting Mo-doped In$_2$O$_3$ thin films, Appl. Surf. Sci. 254 (2008) 4018–4023.
[19] D.S. Bhachu, D.O. Scanlon, G. Sankar, T.D. Veal, R.G. Egdell, G. Cibin, A.J. Dent, C.E. Knapp, C.J. Carmalt, I.P. Parkin, Origin of high mobility in molybdenum-doped indium oxide, Chem. Mater. 27 (2015) 2788–2796.
[20] S. Parthiban, V. Gokulakrishnan, K. Ramamurthi, E. Elangovan, R. Martins, E. Fortunato, R. Ganesan, High near-infrared transparent molybdenum-doped indium oxide thin films for nanocrystalline silicon solar cell applications, Sol. Energy Mater. Sol. Cells 93 (2009) 92–97.
[21] S. Parthiban, K. Ramamurthi, E. Elangovan, R. Martins, E. Fortunato, Spray deposited molybdenum doped indium oxide thin films with high near infrared transparency and carrier mobility, Appl. Phys. Lett. 94 (2009) 2121101.
[22] S. Parthiban, E. Elangovan, K. Ramamurthi, R. Martins, E. Fortunato, High near-infrared transparency and carrier mobility of Mo doped In$_2$O$_3$ thin films for opto-electronics applications, J. Appl. Phys. 106 (2009) 063716.
[23] P.F. Newhouse, C.-H. Park, A. Keszler, J. Tate, P.S. Nyholm, High electron mobility W-doped In$_2$O$_3$ thin films by pulsed laser deposition, Appl. Phys. Lett. 87 (2005) 112108.
[24] M.F.A.M. Van Hest, M.S. Dabney, J.D. Perkins, D.S. Ginley, M.P. Taylor, Titanium-doped indium oxide: a high-mobility transparent conductor, Appl. Phys. Lett. 87 (2005) 2003–2006.
[25] Y. Abe, N. Ishiyama, Titanium-doped indium oxide films prepared by d.c. magnetron sputtering using ceramic target, J. Mater. Sci. 41 (2006) 7580–7584.
[26] R. Hashimoto, Y. Abe, T. Nakada, High mobility titanium-doped In$_2$O$_3$ thin films prepared by sputtering/post-annealing technique, Appl. Phys. Express 1 (2008) 15002.
[27] T. Koida, M. Kondo, Transparent conductive Zr-doped In$_2$O$_3$, Appl. Phys. Lett. 89 (2006) 082104.
[28] T. Koida, M. Kondo, High electron mobility of indium oxide grown on yttria-stabilized zirconia, J. Appl. Phys. 99 (2006) 123703.
[29] T. Koida, M. Kondo, Improved near-infrared transparency in sputtered In$_2$O$_3$-based transparent conductive oxide thin films by Zr-doping, J. Appl. Phys. 101 (2007) 63705.
[30] T. Koida, H. Fujiwara, M. Kondo, Hydrogen-doped In$_2$O$_3$ as high-mobility transparent conductive oxide, Jpn. J. Appl. Phys. 46 (2007) L685–L687.
[31] T. Koida, H. Sai, M. Kondo, Application of hydrogen-doped In$_2$O$_3$ transparent conductive oxide to thin-film microcrystalline Si solar cells, Thin Solid Films 518 (2010) 2930–2933.
[32] S. Nakao, N. Yamada, T. Hitosugi, Y. Hirose, T. Shimada, T. Hasegawa, High mobility exceeding 80 cm^2 V^{-1} s^{-1} in polycrystalline Ta-doped SnO$_2$ thin films on glass using anatase TiO$_2$ seed layers, Appl. Phys. Express 3 (2010) 31102.
[33] N. Yamada, S. Nakao, T. Hitosugi, T. Hasegawa, Sputter deposition of high-mobility Sn$_{1-x}$Ta$_x$O$_2$ films on anatase-TiO$_2$-coated glass, Jpn. J. Appl. Phys. 49 (2010) 108002.
[34] S. Nakao, N. Yamada, T. Hitosugi, Y. Hirose, T. Shimada, T. Hasegawa, Fabrication of transparent conductive W-doped SnO$_2$ thin films on glass substrates using anatase TiO$_2$ seed layers, Phys. Status Solidi C 8 (2011) 543–545.
[35] J.E. Medvedeva, Magnetically mediated transparent conductors: In$_2$O$_3$ doped with Mo, Phys. Rev. Lett. 97 (2006) 086401.
[36] S. Parthiban, E. Elangovan, K. Ramamurthi, R. Martins, E. Fortunato, Investigations on high visible to near infrared transparent and high mobility Mo doped In$_2$O$_3$ thin films prepared by spray pyrolysis technique, Sol. Energy Mater. Sol. Cells 94 (2010) 406–412.
[37] H. Koinuma, I. Takeuchi, Combinatorial solid-state chemistry of inorganic materials, Nat. Mater. 3 (2004) 429–438.
[38] J.G. Lu, T. Kawaharamura, H. Nishinaka, Y. Kamada, T. Ohshima, S. Fujita, ZnO-based thin films synthesized by atmospheric pressure mist chemical vapor deposition, J. Cryst. Growth 299 (2007) 1–10.
[39] T. Kawaharamura, H. Nishinaka, S. Fujita, Growth of crystalline zinc oxide thin films by fine-channel-mist chemical vapor deposition, Jpn. J. Appl. Phys. 47 (2008) 4669–4675.
[40] D. Shinohara, S. Fujita, Heteroepitaxy of corundum-structured α-Ga$_2$O$_3$ thin films on α-Al$_2$O$_3$ substrates by ultrasonic mist chemical vapor deposition, Jpn. J. Appl. Phys. 47 (2008) 7311–7313.
[41] K. Kaneko, T. Nomura, I. Kakeya, S. Fujita, Fabrication of highly crystalline corundum-structured α-(Ga$_{1-x}$Fe$_x$)$_2$O$_3$ alloy thin films on sapphire substrates, Appl. Phys. Express 2 (2009) 075501.
[42] K.-H. Kim, K.-S. Shin, B. Kumar, K.-K. Kim, S.-W. Kim, Mist-CVD growth of high quality ZnO thin films at low temperature for inverted organic solar cells, J. Nanoelectron. Optoelectron. 5 (2010) 247–251.
[43] K. Aikawa, S. Fujita, Electrical conductive corundum-structured α-Ga$_2$O$_3$ thin films on sapphire with tin-doping grown by spray-assisted mist chemical vapor deposition, Jpn. J. Appl. Phys. 51 (2012) 070203.
[44] T. Kawaharamura, T. Uchida, D. Wang, M. Sanada, M. Furuta, Enhancing carrier mobility of IGZO TFT fabricated by non-vacuum mist CVD with O$_3$ assistance, Phys. Status Solidi C 10 (2013) 1565–1568.
[45] H.-J. Jeon, S.-G. Lee, H. Kim, J.-S. Park, Enhanced mobility of Li-doped ZnO thin film transistors fabricated by mist chemical vapor deposition, Appl. Surf. Sci. 301 (2014) 358–362.
[46] K. Sakurai, Atsuo Iida, Fourier analysis of interference structure in X-ray specular reflection from thin films, Jpn. J. Appl. Phys. 31 (1992) L113–L115.

[47] B.H. Freeland, J.J. Habeeb, D.G. Tuck, Coordination compounds of indium. Part XXXIII. X-ray photoelectron spectroscopy of neutral and anionic indium halide species, Can. J. Chem. 55 (1977) 1527–1532.

[48] H.-M. Wu, S.-A. Chen, Dopant-polymer interaction: MoCl$_5$-doped polyacetylene, Synth. Met. 26 (1988) 225–236.

[49] Y. Sawada, C. Kobayashi, S. Seki, H. Funakubo, Highly-conducting indium-tin-oxide transparent films fabricated by spray CVD using ethanol solution of indium (III) chloride and tin (II) chloride, Thin Solid Films 409 (2002) 46–50.

[50] T. Kondo, Y. Sawada, K. Akiyama, H. Funakubo, T. Kiguchi, S. Seki, M.H. Wang, T. Uchida, Step coverage study of indium-tin-oxide thin films by spray CVD on non-flat substrates at different temperatures, Thin Solid Films 516 (2008) 5864–5867.

[51] International Centre for Diffraction Data–ICDD, Powder Diffraction File JCPDS, Philadelphia, PACard No. 06-0416 1997.

[52] International Centre for Diffraction Data–ICDD, Powder Diffraction File JCPDS, Philadelphia, PA, 1997 Card No. 05–0508.

[53] International Centre for Diffraction Data–ICDD, Powder Diffraction File JCPDS, Philadelphia, PACard No. 32–0671 1997.

[54] S.O. Grim, L.J. Matienzo, X-ray photoelectron spectroscopy of inorganic and organometallic compounds of molybdenum, Inorg. Chem. 14 (1975) 1014–1018.

[55] B. Brox, I. Olefjord, ESCA studies of MoO$_2$ and MoO$_3$, Surf. Interface Anal. 13 (1988) 3–6.

[56] W.E. Swartz, D.M. Hercules, X-ray photoelectron spectroscopy of molybdenum compounds. Use of electron spectroscopy for chemical analysis (ESCA) in quantitative analysis, Anal. Chem. 43 (1971) 1774–1779.

[57] G. Seifert, J. Finster, H. Mueller, SW Xα calculations and X-ray photoelectron spectra of molybdenum(II) chloride cluster compounds, Chem. Phys. Lett. 75 (1980) 373–377.

[58] T.A. Patterson, J.C. Carver, D.E. Leyden, D.M. Hercules, A surface study of cobalt-molybdena-alumina catalysts using X-ray photoelectron spectroscopy, J. Phys. Chem. 80 (1976) 1700–1708.

[59] T.H. Fleisch, G.J. Mains, An XPS study of the UV reduction and photochromism of MoO$_3$ and WO$_3$, J. Chem. Phys. 76 (1982) 780–786.

[60] F.A. Kröger, H.J. Vink, Relations between the concentrations of imperfections in crystalline solids, Solid State Phys. 3 (1956) 307–435.

[61] G. Frank, H. Köstlin, Electrical properties and defect model of tin-doped indium oxide layers, Appl. Phys. A Mater. Sci. Process. 27 (1982) 197–206.

[62] N. Yamada, I. Yasui, Y. Shigesato, H. Li, Y. Ujihira, K. Nomura, Donor compensation and carrier-transport mechanisms in tin-doped In$_2$O$_3$ films studied by means of conversion electron ^{119}Sn Mössbauer spectroscopy, Jpn. J. Appl. Phys. 39 (2000) 4158.

[63] I. Hamberg, C.G. Granqvist, Evaporated Sn-doped In$_2$O$_3$ films: basic optical properties and applications to energy-efficient windows, J. Appl. Phys. 60 (1986) R123–R159.

[64] L.L.Y. Chang, B. Phillips, Phase relations in refractory metal-oxygen systems, J. Am. Ceram. Soc. 52 (1966) 527–533.

[65] D. Mergel, Z. Qiao, Correlation of lattice distortion with optical and electrical properties of In$_2$O$_3$: Sn films, J. Appl. Phys. 95 (2004) 5608–5615.

[66] C. Kittel, H. Kroemer, Thermal Physics, Freeman, New York, 1980.

[67] P. Prathap, G.G. Devi, Y.P.V. Subbaiah, V. Ganesan, K.T.R. Reddy, J. Yi, Preparation and characterization of sprayed In$_2$O$_3$:Mo films, Phys. Status Solidi A 205 (2008) 1947–1951.

[68] X. Li, W. Miao, Q. Zhang, L. Huang, Preparation of molybdenum-doped indium oxide thin films using reactive direct-current magnetron sputtering, J. Mater. Res. 20 (2005) 1404–1408.